UCRL-JC-133964
PREPRINT

Molecular Dynamics Simulation of Materials Response to High Strain-Rate Loading

J. Belak

This paper was prepared for submittal to the
International Conference on High Pressure Science and Technology
Honolulu, Hawaii
July 25 - 30, 1999

Manuscript Date (Date report was written)

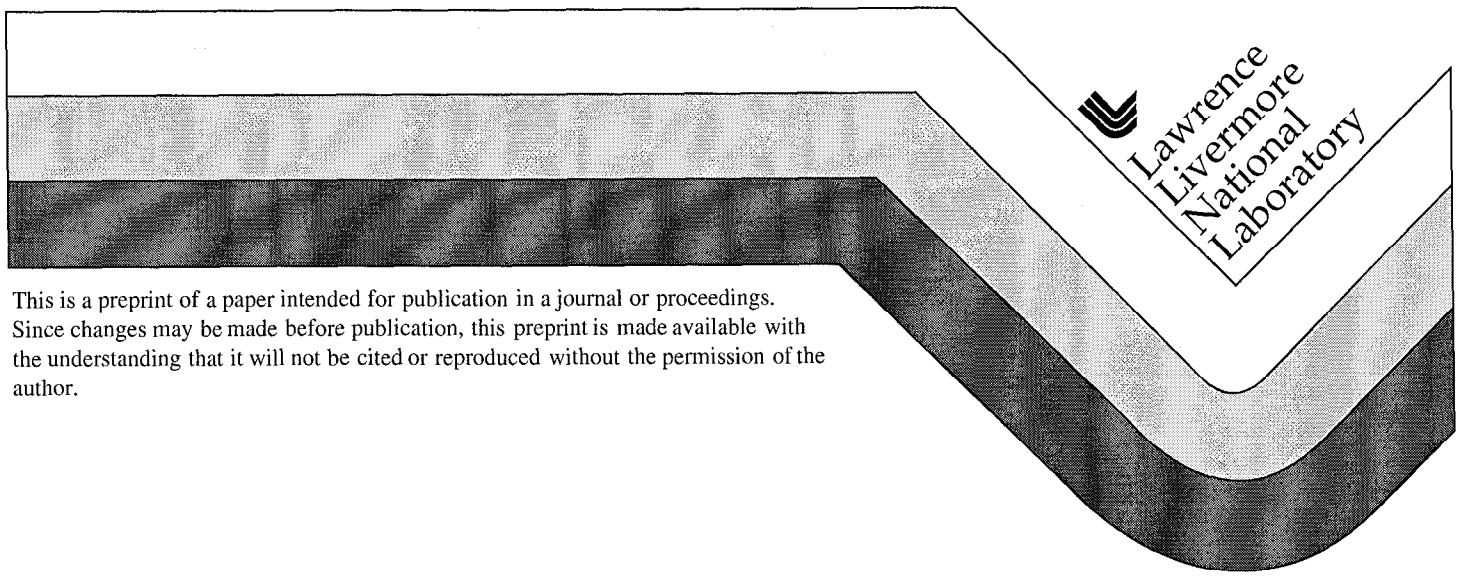

Molecular Dynamics Simulation of Materials Response to High Strain-Rate Loading

James Belak
University of California, Lawrence Livermore National Laboratory, Livermore, CA 94550

A molecular dynamics (MD) analysis of conservation of momentum through a shock front is presented. The MD model uses a non-traditional boundary condition that allows simulation in the reference frame of the shock front. Higher order terms proportional to gradients in the density are shown to be non-negligible at the shock front. The simulation is used to study the sequence of thermodynamic states during shock loading. Melting is observed in the simulations, though above the thermodynamic melt curve as is common in homogeneous simulations of melting. High strain-rate tensile loading is applied to the growth of nanoscale voids in copper. Void growth is found to occur by plasticity mechanisms with dislocations emerging from the void surface.
[molecular dynamics, shock loading, conservation of momentum, shock melting, void growth]

1. Introduction

The molecular dynamics (MD) method has been applied to the study of shock problems with varying degrees of success and has now become a standard technique in the study of atomistic processes at a shock front [1]. In the early work [2-4], the shock was generated by either driving a fixed wall of atoms into a material (material reference frame) or driving a material at a constant velocity into a stationary wall (piston reference frame). More recently, Holian and coworkers [5,6] extended the model by imposing a time-dependent periodic boundary condition to generate the shock within the material frame. However, none of these simulations have been performed within the reference frame of the shock. This latter coordinate frame is especially useful because, in this frame only, the flux of mass ($\rho \boldsymbol{u}$), momentum ($\rho \boldsymbol{uu}+\boldsymbol{P}$) and energy ($\rho \boldsymbol{u}(E+\boldsymbol{uu}/2)+\boldsymbol{uP}+\boldsymbol{q}$) have constant values everywhere when the profile is steady[7]. Here, the macroscopic state variables are as follows: ρ is the mass density, $\boldsymbol{u}$ is the flow velocity, E is the internal energy per unit mass, $\mathbf{P}$ is the pressure tensor (the negative of the stress tensor), and $\boldsymbol{q}$ is the heat current density. Only recently have algorithms been developed to perform the simulation within the reference frame of the shock [8,9], and thus examine in detail the sequence of states which the material experiences during shock loading. In this paper, we examine in detail the conservation of momentum through the shock front and the resulting sequence of states which the material experiences during shock loading. We close with recent results for the high strain-rate growth of microscopic voids as occurs during dynamic fracture (spallation).

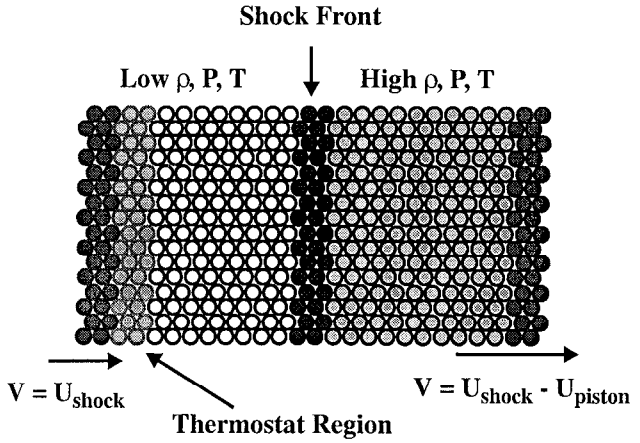

Fig. 1. A schematic illustration of the boundary conditions used to simulate shock propagation within the reference frame of the shock. The molecules flow from left to right in the figure and the shock front is stationary.

2. Methods

During our MD studies of tribological problems [10] we formulated a constant velocity boundary condition for MD simulations. All atoms within a boundary region (see Figure 1) are constrained to propagate at a constant velocity. Atoms are continuously inserted from the left, while atoms that leave the box are discarded—the system is open. The system is initially equilibrated at the desired temperature and density using the standard periodic boundary conditions. The final configuration from this periodic simulation is used to generate the configuration of incoming material. In addition to sampling the incoming velocities from a Maxwell-Boltzmann distribution, we pass this incoming material through a small thermostat region to assure that the initial temperature is as desired. The remaining interior atoms are purely Newtonian and we retain the periodic boundary condition within the plane of the shock. The shock wave simulation is performed by imposing a constant velocity (U_{shock}) to the incoming material and a slower constant velocity (U_{shock}-U_{piston}) to the departing material. As we increase the piston velocity, material piles up at the departing boundary until, above a critical velocity, a sharp density discontinuity propagates into the simulation cell (to the left in Figure 1). We associate this density discontinuity with a shock front. By "tuning" the piston velocity, we make the shock front stationary with respect to the simulation cell and, in doing so, we are able to study shock propagation for arbitrarily long periods of time. Computer animated movies of these simulations demonstrate that the shock front is steady for both solid and fluid simulations. In the simulations presented here we employ cell lengths ranging from 20 to 40 atomic diameters, much greater than the 1-2 atomic diameter shock thicknesses observed for the strong shocks considered [6]. This relatively small cell length allows us to employ large cell widths while simulating no more than a few thousand atoms, hence opening an entire new class of problems to molecular dynamics modeling.

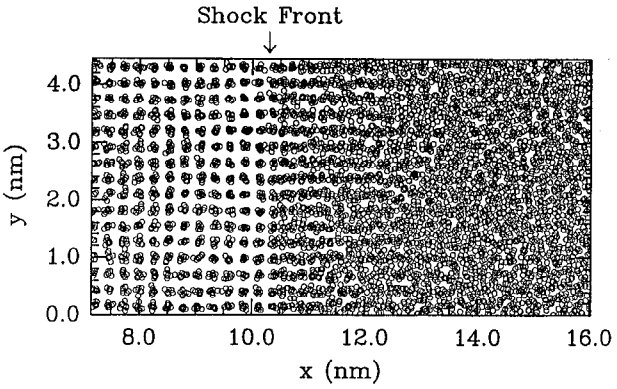

Fig. 2. A "snapshot" (all positions projected onto the x-y plane) of a simulated shock wave propagating along the [100] axis of solid argon at U_{shock}=3.45±.01 km/s and being driven by a piston at U_{piston}=1.27±.01 km/s.

3. Shock Loading of Argon

Figure 2 is a "snapshot" of the system near the shock front from our simulation of a strong shock propagating along the [100] axis in solid argon. The initial conditions were chosen to closely match the experiments of Dick *et. al.*[11] A summary of the potential models employed and initial states simulated in this work is presented in Table I. In these solid-state simulations we find an elastic precursor wave [14] to propagate in front of the plastic shock wave. This elastic wave stagnates at the incoming boundary and the system quickly reaches steady-state. For stronger shocks, the plastic wave overtakes the elastic wave. This appears to be the only observable effect of the constant velocity boundary condition. From the observed disorder and diffusion in the shocked region, we find the final state in Figure 2 to be a fluid at P~7 GPa. We notice an interesting effect. The solid shocks into a dense solid which later melts. We find this to be true for all of the solid shocks presented here—the solid shocks into a solid, which later melts if meta-stable. There is a well defined solid/fluid boundary traveling a few nanometers behind the shock front in Figure 2. From the observed shock (3.45±.01 km/s) and piston (1.27±.01 km/s) velocities for this simulation, we estimate the time to undergo the melting transition to be a few picoseconds.

To facilitate comparison with experiment, we have introduced cross-sectional bins (1000 per simulation cell) into which to measure physical observables. For the simulation

TABLE 1. Summary of potential models and initial states used to simulate shocked argon.

Lennard-Jones potential [12]: ε=119 K, σ=3.405 Å
Exponential-6 potential [13]: ε=122 K, r_o=3.85 Å, α=13.2
Initial states simulated (ρ) for exponential-6 potential model):

solid:	T=75 K, P=0, ρ=1.567±.001 gms/cm^3
liquid:	T=90 K, P=0, ρ=1.399±.001 gms/cm^3

System parameters:

system size (N)	2000-10000 atoms
time-step (reduced units)	0.0025-0.005
simulation time	2600-10400 time-steps
cross-sectional area	8.25-75 nm^2

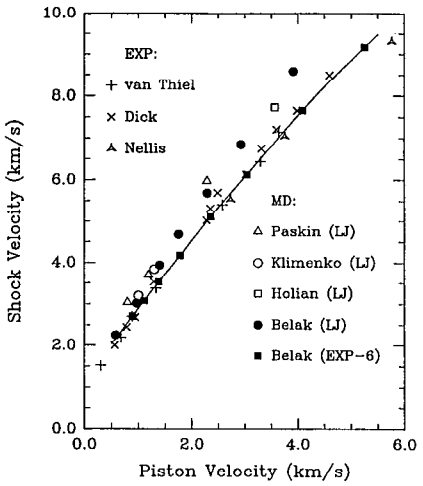

Fig. 3. The observed shock velocity as a function of piston velocity for simulated solid argon with the shock propagating along the [100] axis. The smooth curve is drawn through the simulation data and serves as a guide to the eye.

shown in Figure 2, the width of each bin is ~0.018 nm. There is no ambiguity in using bin widths this small as they are fixed relative to the shock and the material flows through the bin. The averages presented here are relative (in position) to the shock front. One observable of primary interest is the average flow velocity. We find the velocity to maintain a well-defined plateau (U_{shock}) in front of the shock, decreasing rapidly through the shock front, and maintaining a well-defined plateau (U_{shock}-U_{piston}) well behind the shock. A plot of U_{shock} versus U_{piston} for shocks along the [100] axis in solid argon is shown in Figure 3. Also shown are experimental results on solid [11] and liquid [15,16] argon and a selection of previous MD simulation data [3,4,5]. The new results are in quantitative agreement with the previous simulations and the exponential-6 potential is shown to be a more faithful representation of the experimental data.

Having shown that our simulations model the experiments reasonably well, we turn our attention to the transport of mass and momentum through the shock front. We find the convective mass flux (ρu) to be constant (independent of position) to within our statistical uncertainty, which arises primarily from the uncertainty in our measurement of the density. Shown in Figure 4 is the average longitudinal pressure (P_{xx}), convective momentum flux (ρu^2), and the total momentum flux as a function of position for the simulation described in Figure 2. The oscillatory features in P_{xx} and ρu^2 are characteristic of the crystalline structure of the solid and are steady down to the shortest subaverage considered (a few vibrational periods). We do not observe them in our liquid state simulations.

A general expression for the pressure tensor ($\underline{\boldsymbol{P}}(\boldsymbol{r}) = \underline{\boldsymbol{P}}_K(\boldsymbol{r}) + \underline{\boldsymbol{P}}_V(\boldsymbol{r})$), valid for arbitrary density inhomogeneities, was derived by Irving and Kirkwood [17]:

$$P_{K,\alpha\beta}(\boldsymbol{r}) = \left\langle \sum_{i=1}^{N_{bin}} m(\boldsymbol{v}_i - \boldsymbol{u}_{bin})_\alpha (\boldsymbol{v}_i - \boldsymbol{u}_{bin})_\beta \delta(\boldsymbol{r}_i - \boldsymbol{r}) \right\rangle$$

and

$$P_{V,\alpha\beta}(\boldsymbol{r}) = -\langle \frac{1}{2}\sum_{i}^{N_b}\sum_{j}^{N_s} f_{\alpha\beta}(r_{ij})\left\{1-\frac{1}{2}\boldsymbol{r}_{ij}\bullet\nabla_r+\ldots\right\}\delta(\boldsymbol{r}_i-\boldsymbol{r})\rangle$$

where $\boldsymbol{u}_{bin}$ is the average flow velocity, <> denotes an ensemble average and

$$f_{\alpha\beta}(r_{ij}) = \frac{\partial\varphi(r_{ij})}{\partial r_{ij}}\frac{(\boldsymbol{r}_{ij})_\alpha(\boldsymbol{r}_{ij})_\beta}{r_{ij}}.$$

Massignon [18] has derived an integral expression that avoids the above expansion:

$$P_{V,\alpha\beta}(\boldsymbol{r}) = -\langle \frac{1}{2}\sum_{i}^{N_b}\sum_{j}^{N_s} f(r)\int_0^1 ds\,\delta(\boldsymbol{r}-\boldsymbol{r}_i-s(\boldsymbol{r}_j-\boldsymbol{r}_i))\rangle,$$

which has been discussed in the context of surface tension [19] and shock physics [20]. Common practice is to include only the first term in the expansion for the virial, valid when the material is homogeneous. The resulting longitudinal pressure is shown as the dashed curve in Figure 4c. Adding the convective momentum flux, we find the dashed curve in Figure 4a. The oscillatory features, though only a few percent of the total momentum flux, are well beyond the statistical uncertainty in the calculation. These features are due to neglect of higher order terms in the expansion—terms proportional to gradients in the density.

In the appendix to their paper, Irving and Kirkwood showed that by considering the force acting across a fixed surface in the material, they obtain an integral expression over the pair density equivalent to the integral expression of Massignon. Upon Taylor expansion, they showed that their integral expression is equivalent to their previous expansion. Following Irving

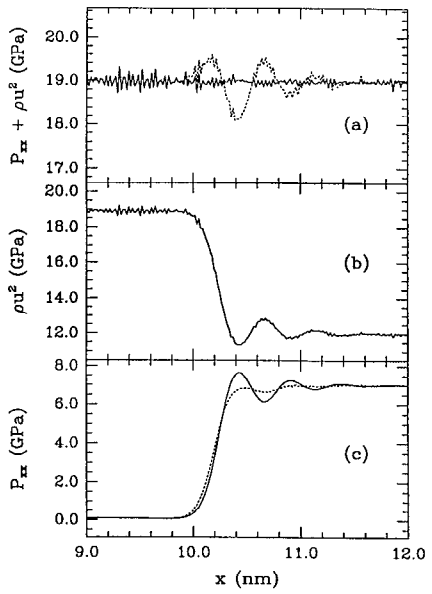

Fig. 4. (a) The total momentum flux, (b) the convective momentum flux (ρu^2), and (c) longitudinal component of the pressure tensor ($\boldsymbol{P}_{xx}$) as a function of position through the shock front for the simulation described in Figure 2.

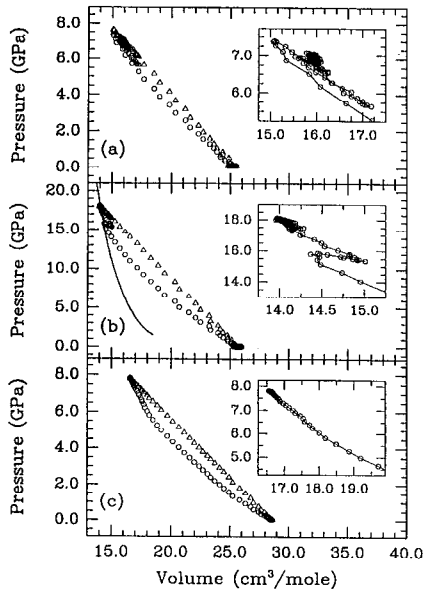

Fig. 5. The sequence of states in P-V space that the system follows as it goes through the shock front. (a) The shock described in Figure 2.(b) A solid-state shock at U_{shock} = 5.060±.005 km/s being driven at U_{piston}=2.27±.02 km/s. The smooth curve is the calculated solid Hugoniot (locus of final PV states). (c) A liquid-state shock at U_{shock}=3.651±.003 km/s being driven at U_{piston}=1.526±.005 km/s. In each case, the inset shows the sequence of P-V states as the system approaches the final state.

and Kirkwood, we introduce fixed surfaces (the plane at the center of each bin) and explicitly evaluate the ensemble average of all interatomic forces across this fixed plane. The resulting longitudinal pressure is shown as the solid curve in Figure 4c. Adding the convective momentum flux, we obtain the solid curve in Figure 4a—momentum is conserved to within our statistical uncertainty, as expected.

Having demonstrated that our calculation of the pressure tensor correctly conserves momentum, we now examine the sequence of thermodynamic states through which the material transforms during shock loading. In Figure 5, we show the path in P-V space for three simulations. The open triangles represent the longitudinal component of the pressure tensor ($\boldsymbol{P}_{xx}$) which varies linearly with volume through the shock front. This straight line is known as the Rayleigh line and the area beneath this line is equal to the change in internal energy between the initial and final states [7]. The pressure, however, includes both the longitudinal and transverse components of the pressure tensor ($P = (P_{xx} + P_{yy} + P_{zz}) / 3$) and the sequence of pressure states (open circles) does not vary linearly with volume.

The sequence of pressure states for the simulation described in Figure 2 is shown in Figure 5a. At the shock front, the pressure over-shoots the final state, then oscillates with diminishing amplitude, finally rising slightly at nearly constant volume as the system melts. In Figure 5b, we show the sequence of states for a stronger shock (18 GPa) in the solid. The pressure, while increasing in the solid, does not over-shoot the final state

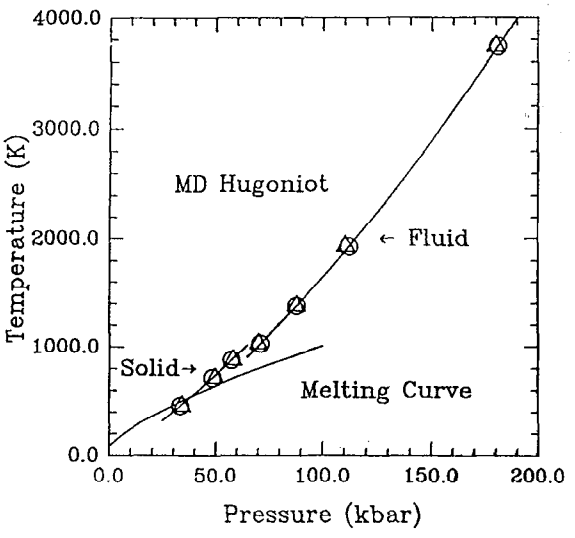

Fig. 6 Simulated Hugoniot of argon in Temperature-Pressure. The initial condition is a solid at the experimental conditions [11] and the shock is propagating along the [100] direction is the fcc crystal. The melting curve is taken from reference 13.

and the melting does not occur at constant volume. We also show in this figure, for comparison, our calculated Hugoniot curve (locus of final PV states) for shocks along the [100] axis in solid argon. Finally, we show in Figure 5c, the sequence of states for a liquid-state shock of similar strength to the solid-state shock shown in Figure 5a. The pressure rises smoothly with decreasing volume, though we note a slight kink in the curve near the final state, possibly due to the fluid responding in a solid-like manner during the short time scale involved in loading and later relaxing out of the non-equilibrium state.

The calculated Hugoniot for argon in temperature and pressure is shown in Figure 6 using the exponential-6 interatomic force model. The temperature is calculated from the expectation value of the kinetic energy far behind the shock front after equilibrium has been attained. The pressure is calculated two ways: (1) from the Hugoniot relations and (2) from the expectation value of the stress tensor. The agreement between the two calculations is quite good. In contrast to recent MD simulations [21], melting along the Hugoniot in this work occurs above the thermodynamic transition for this potential [13], as is common in MD simulations of homogeneous melting.

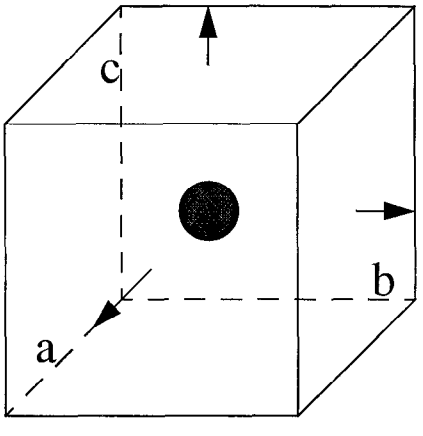

Fig. 7. Isotropic tension is simulated by expanding the simulation cell in all directions at a constant rate. A nanoscale void of size R = 2nm $\approx l_{cell}/10$ is cut from the center of the cell.

4. High Strain-Rate Void Growth

The growth of microscopic voids is fundamental to the ductile fracture of metals [22]. At high strain-rates, as occur during shock loading, there is insufficient time for diffusive processes and void growth occurs by plasticity mechanisms. The long history of experiment [23] and of continuum plasticity models of void growth [22,24-27] has resulted in a highly successful continuum computer code model of failure based on the nucleation and growth of voids [28-30]. However, there remains many unanswered questions concerning the microscopic mechanisms of void nucleation and plastic growth.

A cubic simulation cell containing N=864000 atoms was created by replicating 60 FCC unit cells along each of the cubic axes. The embedded-atom method [31,32] is used to model copper. The equations of motion are integrated using a Verlet leap-frog algorithm with a time step of 6fs and periodic boundary conditions [12]. The system was simulated at T=300K and P=0 to an equilibrium cell length of l_{cell} = 21.7nm. A void of radius 2nm was then cut from the center of the simulation cell as shown schematically in Figure 7, resulting in a system containing N=860396 atoms. The positions of every atom in the simulation cell are rescaled as is commonly done in constant pressure MD simulations [33]: where, $\underset{\sim}{x} = H\underset{\sim}{s}$, $s \subset [0, 1]$, and $H = \{\underset{\sim}{a}, \underset{\sim}{b}, \underset{\sim}{c}\}$ is a matrix composed of the simulation cell vectors. An isotropic constant strain-rate is simulated by specifying a constant time derivative of H. After equilibrium, the thermostat is turned off and expansion is simulated under adiabatic conditions.

In a seminal paper on dynamic fracture, Barbee *et.al* [28] measured the growth rate of microscale voids in copper. They observed a viscous growth law of the form:

$$V = V_o e^{\frac{3(\sigma - \sigma_{go})}{4\eta} t} = V_o e^{\alpha t}$$

where V is the void volume, σ is the applied stress, $\sigma_{go} = 0.005$ GPa is the growth threshold stress, and $\eta = 0.2$ Pa·s is a material viscosity. At an applied stress of 6 GPa (well outside the experimental data), this model predicts a growth exponent of $\alpha \approx 2.2\times10^{10}s^{-1}$.

Comparison with the MD data requires a metric of the void volume within the MD simulation. A void is where the atoms are not. Thus, we define a background grid and compute the sum of unoccupied grid zones. A grid spacing smaller than an atom size leads to spurious results. We find l_{grid} = 0.36nm gives reproducible results consistent with the known initial void radius (2nm). This void volume metric introduces an error which scales as 1/R. We estimate the error to be no more than a few percent for R = 2nm. The resulting volume is shown in Figure 8 as a function of simulation time. Three distinct, nearly

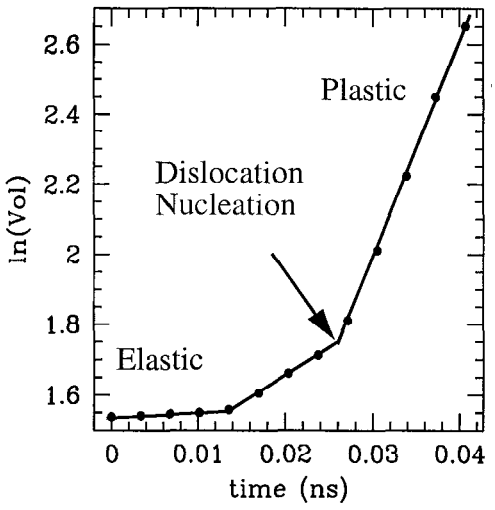

Fig. 8. The natural log of the void volume as a function of time for growth of an R=2nm void. The lines are drawn as a guide to the eye.

linear regions are observed on the log plot, suggesting exponential growth. Void growth at early time is elastic, displaying no change when normalized by the total system volume. At late time, the growth is fully plastic with a surrounding network of dislocations moving into the material. Dislocations, as shown in Figure 9, first emerge from the void surface at t≈0.025ns and the nature of the intermediate region is not clear. From the slope of the curve at late time we estimate the growth exponent in the simulation to be $\alpha \approx 6.2\times10^{10}s^{-1}$. The factor of three higher exponent than expected from experiment is likely due either to the vast difference in length scale between the simulation and experiment, the surrounding perfect crystal in the MD simulation, or the empirical nature of the interatomic potential model. Further details may be found in reference 34.

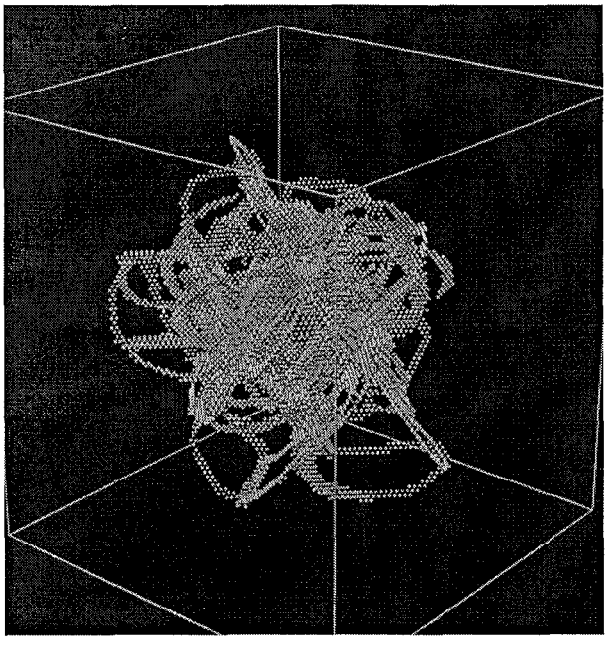

Fig. 9. The defect structure at t=0.030ns as revealed by the atoms with potential energy 1% above the bulk potential energy at T = 1K.

5. Summary

A molecular dynamics analysis of conservation of momentum through a shock front is presented. The MD model uses a non-traditional boundary condition that allows simulation in the reference frame of the shock front. Higher order terms proportional to gradients in the density are shown to be non-negligible at the shock front. The simulation is used to study the sequence of thermodynamic states during shock loading. Melting is observed in the simulations, though above the thermodynamic melt curve as is common in homogeneous simulations of melting. High strain-rate tensile loading is applied to the growth of nanoscale voids in copper. Void growth is found to occur by plasticity mechanisms with dislocations emerging from the void surface.

6. Acknowledgments

The author is indebted to Marvin Ross, Dave Boercker, Matt van Thiel, Neil Holmes, Roger Minich, and Hector Lorenzana for many useful suggestions and enlightening discussions. This work was performed at Lawrence Livermore National Laboratory under the auspices of the U.S. DOE through Contract No. W-7405-ENG-48.

7. References

[1] B.L. Holian, Shock Waves **5**, 149 (1995).
[2] D.H. Tsai and C.W. Beckett, J. Geophys. Res. **71**, 2601 (1966).
[3] A. Paskin and G.J. Dienes, J. Appl. Phys. **43**, 1605 (1972).
[4] V.Yu. Klimenko and A.N. Dremin, Sov. Phys. Dokl. **25**, 288 (1980).
[5] B.L. Holian, W.G. Hoover, B. Moran, and G.K. Straub, Phys. Rev. A **22**, 2798 (1980).
[6] B.L. Holian, Phys. Rev. A **37**, 2562 (1988).
[7] Ya. B. Zel'dovich and Yu. P. Razier, *Physics of Shock Waves and High-Temperature Hydrodynamic Phenomena* (Academic Press, New York, 1966).
[8] J. Belak, in *High-Pressure Science and Technology-1993*, S.C. Schmidt, J.W. Shaner, G.A. Samra, and M. Ross eds. (APS Press, New York, 1994).
[9] S.I. Anisimov, V.V. Zhakhovskii, and V.E. Fortov, JETP Lett. **65**, 755 (1997).
[10] J. Belak and I.F. Stowers, in *Fundamentals of Friction*, I.L. Singer and H. Pollock eds. (Kluwer, Dordrecht, 1992).
[11] R.D. Dick, R.H. Warnes, and J. Skalyo, Jr., J. Chem. Phys. **53**, 1648 (1970).
[12] For a review of MD methods and simple potentials see M.P. Allen and D.J. Tildesley, *Computer Simulation of Liquids*, (Clarendon Press, Oxford, 1987) and D.W. Heermann, *Computer Simulation Methods in Theoretical Physics, 2nd ed.*, (Springer-Verlag, Berlin, 1990).
[13] M. Ross, H.K. Mao, P.M. Bell, and J.A. Xu, J. Chem. Phys. **85**, 1028 (1986).
[14] See for example D.C. Wallace, Phys. Rev. B **22**, 1487 (1980).
[15] M. Van Thiel and B.J. Alder, J. Chem. Phys. **44**, 1056 (1966).

[16] W.J. Nellis and A.C. Mitchell, J. Chem. Phys. **73**, 6137 (1980).
[17] J.H. Irving and J.G. Kirkwood, J. Chem. Phys. **18**, 817 (1950).
[18] D. Massignon, *Mecanique Statisique des Fluids* (Dunod, Paris, 1957).
[19] P. Schofield and J.R. Henderson, Proc. Roy. Soc. A **379**, 231 (1982).
[20] R.J. Hardy, J. Chem. Phys. **76**, 622 (1982).
[21] A.B. Belonoshko, Science Mag. **275**, 955 (1997).
[22] A.S Argon ed., *Topics in Fracture and Fatigue*, (Springer-Verlag, New York, 1992).
[23] J.S. Rinehart and J. Pearson, *Behavior of Metals Under Impulsive Loads*, (ASME, Cleveland, 1954, reprinted by Dover, New York, 1965).
[24] F.A. McClintok, *J. Appl. Mech.* **35**, 363 (1968).
[25] J.R. Rice and D.M. Tracy, *J. Mech. Phys. Solids* **17**, 201 (1969).
[26] A. Needleman, *J. Appl. Mech.* **39**, 964 (1972).
[27] A.L. Gurson, *J. Eng. Mater. Tech.* **99**, 2 (1977).
[28] T.W. Barbee, Jr., L. Seaman, R. Crewdson, and D. Curran, *J. Materials* **7**, 393 (1972).
[29] D.R. Curan, L. Seaman, and D.A. Shockey, *Phys. Rep.* **147**, 253 (1987).
[30] M.A. Meyers and C.T. Aimone, *Prog. Mater. Sci.* **28**, 1 (1983).
[31] M.S. Daw and M.I. Baskes, *Phys. Rev. B* **29**, 6443 (1984).
[32] D.J. Oh and R.A. Johnson, p233 in *Atomistic Simulation of Materials: Beyond Pair Potentials*, V. Vitek and D.J. Srolovitz eds., (Plenum, New York, 1989).
[33] M. Parrinello and A. Rahman, *J. Appl. Phys* **52**, 7182 (1981).
[34] J. Belak, J. Comp-Aided Mater. Design **5**, 193 (1998).